Diamond & Related Materials 166 (2026) 113713

Contents lists available at ScienceDirect

Diamond & Related Materials

journal homepage: www.elsevier.com/locate/diamond

Three-dimensional variable range hopping transport in hydrogen-free amorphous carbon films: Role of sp^2 cluster size

Jingyun Feng [a,b], Peng Guo [a,*], Hao Li [a], Rende Chen [a], Aiying Wang [a,b,**]

[a] State Key Laboratory of Advanced Marine Materials, Zhejiang Key Laboratory of Extreme-environmental Material Surfaces and Interfaces, Ningbo Institute of Materials Technology and Engineering, Chinese Academy of Sciences, 315201, Ningbo, China
[b] Center of Materials Science and Optoelectronics Engineering, University of Chinese Academy of Sciences, 100049, Beijing, China

ARTICLE INFO

Keywords:
H-Free amorphous carbon
Cluster size
Electrical behaviors
Three-dimensional variable range hopping

ABSTRACT

Amorphous carbon (a-C) films have garnered considerable attention as promising semiconductor materials for next-generation electronic devices owing to their exceptional electrical properties. However, the carrier transport mechanism of amorphous carbon films remains poorly understood, primarily attributed to their atomic structural complexity and diverse electrical behaviors. In this study, hydrogen-free amorphous carbon films were fabricated via high-power impulse magnetron sputtering. By precisely controlling the applied bias voltage, a stable sp^2 content of approximately 52% was maintained while the sp^2 cluster size (L_a) was varied from 1.63 to 1.93 nm. This approach enabled a systematic investigation of the correlation between the nanostructure and the resultant electrical properties. All a-C films exhibited n-type conduction with a stable electron concentration of 2.1×10^{18} cm^{-3}. Their resistivity spanned 0.3–8.7 Ω·cm, and films with larger L_a values and higher structural ordering demonstrated reduced resistivity, attributed to enhanced electron mobility. Electrical transport measurements conducted over a temperature range of 100 to 350 K confirmed that charge transport is governed by a three-dimensional variable range hopping mechanism. Electron hopping between adjacent sp^2 clusters predominantly dictates the electrical properties. This work provides critical insights into the structure-property relationships of a-C films and offers important theoretical and experimental support for the design and development of next-generation carbon-based electronic devices.

1. Introduction

Owing to their exceptional combination of properties, amorphous carbon (a-C) films and their hydrogenated counterparts (a-C:H) have emerged as important protective and multifunctional coating materials. These include high hardness, superior chemical inertness, exceptional smoothness, and excellent wear resistance [1–6]. In addition, as amorphous semiconductor materials, their electrical properties are tunable from insulators to conductors, which renders them promising candidates for next-generation electronic devices, such as wearable strain sensors, resistive random-access memory (RRAM) devices, and micro-electromechanical systems (MEMS) [7–15].

Significant research efforts have recently been devoted to elucidating the underlying charge transport mechanisms in these materials. Based on analyses of temperature-dependent conductivity, Bhattacharyya and Silva [16] comprehensively reviewed the charge transport mechanisms operative in various a-C and a-C:H films, which include the Arrhenius type, variable range hopping (VRH), multiphonon tunneling, activated type or a combination of extended state plus hopping. Subsequently, many researchers also confirmed that variations in the H content, the sp^2/sp^3 ratio, and the sp^2 cluster size can cause various transport behaviors [17,18]. For example, in the a-C:H film, Katamune et al. [19] observed that increasing the H concentration induced a transition from semi-metallic to semi-conducting properties. Zhai and co-workers [20] further noted that increasing the sp^2/sp^3 ratio led to a monotonic enhancement in conductivity. However, Dwivedi et al. [21] reported contradictory results showing that the conductivity of the a-C:H film initially decreased and then increased as the sp^2/sp^3 ratio increased from 0.42 to 0.67. Compounding this complexity, even in the H-free a-C film, the conductivity is also influenced by the sp^2 cluster size and the

* Corresponding author.
** Correspondence to: A. Wang, State Key Laboratory of Advanced Marine Materials, Zhejiang Key Laboratory of Extreme-environmental Material Surfaces and Interfaces, Ningbo Institute of Materials Technology and Engineering, Chinese Academy of Sciences, 315201, Ningbo, China.
E-mail addresses: guopeng@nimte.ac.cn (P. Guo), aywang@nimte.ac.cn (A. Wang).

https://doi.org/10.1016/j.diamond.2026.113713
Received 6 March 2026; Received in revised form 19 April 2026; Accepted 4 May 2026
Available online 5 May 2026

sp^2/sp^3 ratio [22]. Additionally, both p-type [20,23–25] and n-type conduction [25–27] were identified in a-C and a-C:H films, which were often overlooked in carbon-based electronic devices.

Overall, prior studies have proposed that at least three key factors—the H content, the sp^2/sp^3 ratio, and the sp^2 cluster size—significantly influence the electrical properties of amorphous carbon (a-C) films. To date, however, the transport mechanism of a-C films remains poorly elucidated; limited progress has been made in understanding the roles of these individual factors, which has emerged as a major bottleneck for designing advanced carbon-based electronic devices [7,10,16].

In the present study, H-free a-C films were fabricated using high-power impulse magnetron sputtering (HiPIMS). Stable sp^2 content and varying the sp^2 cluster size (L_a) were tailored by adjusting the applied bias voltage. The electrical behaviors and related transport mechanism of a-C films were investigated. Herein, the underlying relationship between the sp^2 cluster size (L_a) and the electrical behavior of a-C films is elucidated, providing both theoretical and experimental support for the design of high-performance carbon-based electronic devices.

2. Experimental details

2.1. Sample preparation

The a-C films were deposited by a DC-superimposed high-power impulse magnetron sputtering technique (HiPIMS, P600–1) [28–30]. This system is equipped with a 99.99% pure graphite target, which can provide a significantly higher ionization fraction of sputtered vapor compared to that of traditional sputtering systems.

P-type Si (100) wafers, quartz plates, and Al_2O_3 (0001) substrates were used for specific characterizations. Specifically, Si (100) wafers were utilized for the analysis of thickness, surface morphology (AFM and SEM), chemical composition (XPS and Raman), microstructure (TEM). Meanwhile, quartz plates were primarily employed for electrical measurements under room temperature conditions, including resistivity and Hall-effect, Al_2O_3 (0001) substrates were used for I-V characteristics and temperature-dependent conductivity tests (100 to 350 K).

Prior to a-C film deposition, all substrates were ultrasonically cleaned sequentially in acetone and alcohol for 15 min, then fixed in the deposition chamber.

When the base pressure was evacuated to approximately 3×10^{-3} Pa, all substrates were etched with Ar^+ ions for 30 min to remove surface contaminants.

During deposition, the DC magnetron sputtering current was maintained at 1.0 A. The pulse frequency, pulse width, and voltage of the HiPIMS unit were 300 Hz, 65 μs, and 1000 V, respectively. Pulsed bias applied to the substrates was maintained at 0 V (floating state), −50 V, −100 V, −200 V, and -300 V.

2.2. Characterization

Their thickness was measured from step edges using the surface profilometer (Alpha-Step IQ, US). Their surface topography and roughness were characterized by the atomic force microscopy (AFM, Dimension 3100 V, Veeco, US), the images (1 μm × 1 μm) were recorded in tapping mode, and corresponding root-mean-square roughness (Rq) values were calculated.

The chemical composition was characterized by X-ray photoelectron spectroscopy (XPS, Axis Ultra DLD, Japan) using monochromatic Al (mono) Kα radiation at a pass energy of 160 eV. Prior to measurement, the analyzed area was cleaned via 2 keV Ar^+ ion sputtering for 3 min to remove impurities and surface adsorbents. The sp^2 content was determined from the C 1 s XPS spectra, with a mixed fitting of a Gaussian (20%) function and a Lorentzian (80%) function used to fit the sp^2-C peak and sp^3-C peak after Shirley background subtraction [29,30]. The structural characterization of the a-C films was investigated by the multiwavelength Raman spectroscopy (Renishaw in Via Reflex, 532 nm and 325 nm) with a detection range of 900 to 2000 cm^{-1}. The microstructure of the a-C film deposited at −50 V was characterized by the high-resolution transmission electron microscopy (TEM, Tecnai F20, US) at an acceleration voltage of 200 kV. The sample for cross-sectional TEM analysis was prepared using the focused ion beam (FIB, Carl Zeiss, Auriga) with electron imaging and Ga-ion milling capabilities.

The carrier concentration and mobility of the a-C films were measured by the Hall-effect measurement (Nanometrics, HP-5500C, US) in a Van der Pauw configuration [32]. All samples were deposited on square quartz glass substrates, with Pt films around 15 nm deposited as contact electrodes at four corners via electron beam evaporation. Their room-temperature resistivity and current-voltage (I-V) characteristics were tested by the semiconductor parameter analyzer (Keithley 4200 SCS, US). The temperature dependence of the electrical properties of the a-C films was measured by physical property measurement system (PPMS, Quantum Design, Model-9) using a standard four-probe method, with the test temperature range of 100 to 350 K.

3. Results and discussion

3.1. Thickness, morphology and mechanical properties

Table 1 presents the detailed deposition parameters, including thickness and Rq of the a-C films. From 0 to −100 V, the average growth rate was approximately 3 nm/min, and the thickness of the a-C films was maintained around 200 ± 30 nm.

Fig. 1 illustrates the 1 μm × 1 μm 2D-AFM images and the corresponding 3D-AFM images of the a-C films at various substrate biases. Overall, all a-C films showed a smooth surface, with Rq (Table 1) less than 1.5 nm. As the bias increased from 0 to −300 V, the surface became flatter and more featureless. At the lower bias range of 0 to −100 V, many cauliflower-like structures with lateral sizes of approximately 40–100 nm were observed. With further increasing bias to −300 V, these coarse grains became smaller and scrubbier, and the corresponding Rq exhibited an obvious decreasing trend from around 1.2 nm to 0.19 nm. The evolution of the surface morphology can be explained as follows. At the lower bias, the growth of a-C film took place under diffusion limited conditions, resulting in its relatively rough surface [31]. Then, with the increase of the bias voltage, the incoming ions had a higher energy, which induced an efficient lateral transport process during film growth, resulting in its ultra-smooth surface [5,34,35].

3.2. Chemical composition and structure

For all a-C films, only argon, carbon, oxygen and nitrogen elements were detected with XPS, as shown in Fig. 2a. The small amounts of N and O atoms (less than 2.8 at.%) may originate from the oxidization or adsorption of water vapor on the sample surface during or after film deposition [34,36]. Fig. 2b presents the fitted sp^2 content from XPS C1s spectra. After deconvoluting the XPS C1s spectra (insets in Fig. 2b) into two peaks [32], the C═C peak at 284.6 eV (sp^2 bond) and the C—C peak at 285.8 eV (sp^3 bond) were identified. The sp^2 content in a-C films can be empirically derived based on the ratio of the corresponding peak areas [33]. Different from the previous results [2,34,37], the sp^2 content of the a-C films remained approximately 52% regardless of substrate bias variations within the 0 to −300 V range.

Fig. 3 shows two-wavelength (visible-ultraviolet) Raman spectra of the a-C films. At both 532 nm and 325 nm, a broad asymmetric peak was observed for each sample, demonstrating typical features of amorphous carbon. To gain insights into the bond arrangements, the spectra were fitted with two Gaussian peaks corresponding to the D and G peaks [38,39]. The G peak position, the full width at half maximum of the G peak (G FWHM), the integrated intensity ratio (I_D/I_G) and G peak dispersion can be deduced.

Table 2 presents the fitting results of the Raman spectra obtained at

Table 1
Deposition parameters, thickness and Rq of the a-C films.

HiPIMS	Direct-current (A)	Ar flow (sccm)	Deposition time (min)	Substrate bias (V)	Rq (nm)	Thickness (nm)
Pulse voltage 1000 V	1.0	50	65	0	1.0	176
Pulse frequency 300 Hz				−50	1.3	197
Pulse width				−100	1.3	231
65 μs				−200	0.5	198
				−300	0.2	200

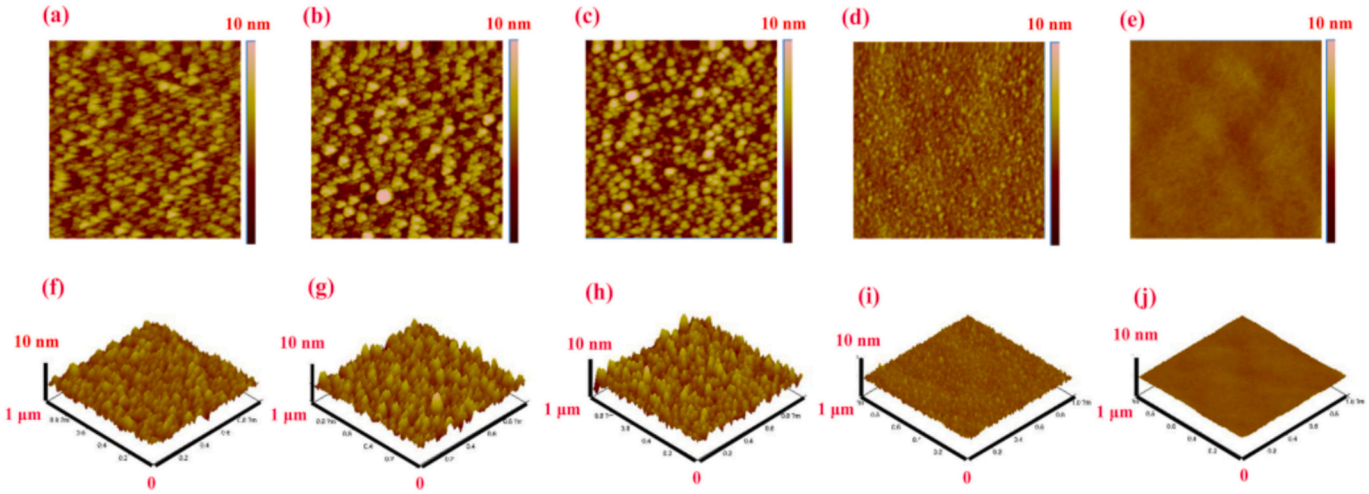

Fig. 1. The tapping mode 2D-AFM images (a), (b), (c), (d), (e) (the right scales represent the height), and the corresponding 3D-AFM images (f), (g), (h), (i), (j) of the a-C films at 0, −50 V, −100 V, −200 V and -300 V.

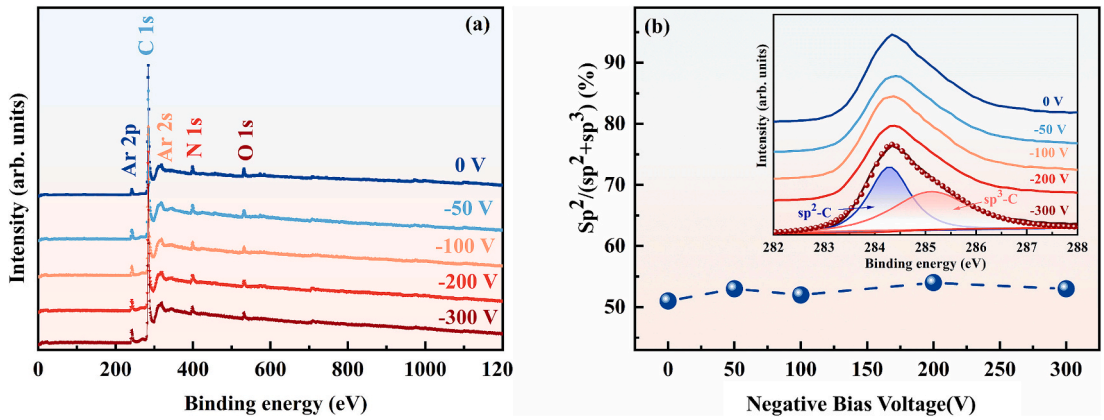

Fig. 2. (a) XPS spectra of the a-C films at various biases and (b) fitted sp^2 content from XPS C1s spectra. The inset in Fig. 2 (b) exhibits C1s peak of the a-C films.

532 nm. As the bias varied from 0 to −300 V, the G peak position remained at approximately 1547 cm^{-1}, implying a stable sp^2 content, which was consistent with XPS results. The G FWHM increased evidently from 178.5 to 191.4 cm^{-1}, indicating the rise of structural disorder. It was noted that I_D/I_G first increased from 1.73 to its maximum value of 2.05 at −50 V, then declined to around 1.5 with further increase of the applied bias. For visible Raman spectra, clustering in the a-C films is the primary factor that influences the I_D/I_G; consequently, the sp^2 cluster size (L_a) can be roughly estimated via the following equation, on the premise that L_a is under 20 Å [39–41],

$$I_D \Big/ I_G = C^{'}(\lambda)^2 \tag{1}$$

where λ is the excitation wavelength (532 nm), and C' is the variable scaling factor (~0.55 nm^{-2}) in this case. The corresponding L_a values were 1.77 nm at 0 V, 1.93 nm at −50 V, 1.87 nm at −100 V, 1.63 nm at −200 V, and 1.72 nm at −300 V, respectively.

From the visible and ultraviolet (UV) excitation measurements, the G peak position of all samples increased as the excitation wavelength decreased. Furthermore, the G peak dispersion, defined as the rate of change of the G peak position and change of the excitation wavelength, ranged from 0.09 to 0.23 cm^{-1}/nm, as shown in the Table 2. Since the G peak dispersion increases with disorder, the sample deposited at −50 V had the highest ordering and the sample at −200 V exhibited the largest topological disorder. Besides, all a-C films had a similar G position in visible Raman spectra but differed in the UV Raman spectra. Consequently, the two samples deposited at −100 V and 300 V with the mild G peak dispersion also had more sp^2 clustering. [39–41].

Fig. 4a and b display the typical cross-sectional TEM image, high resolution transmission electron microscopy (HRTEM) and the

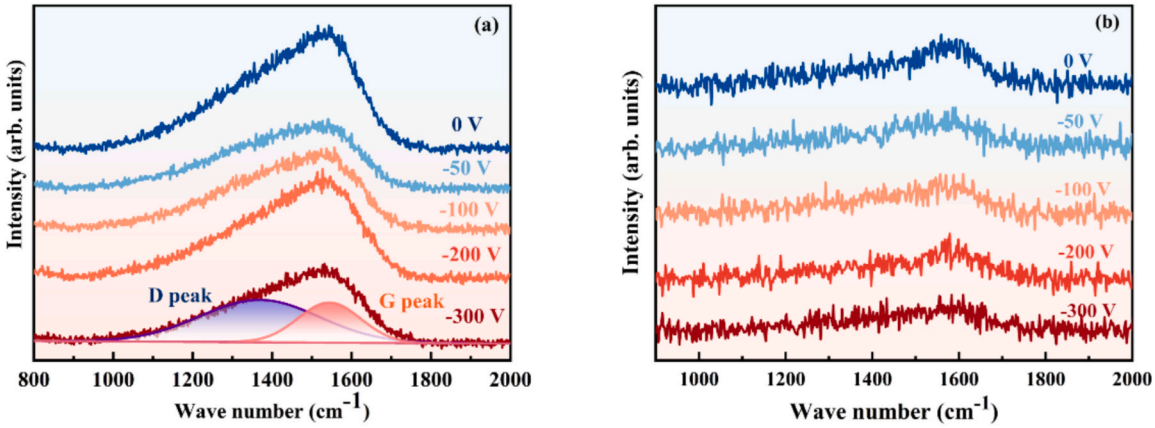

Fig. 3. Raman spectra of a-C films at wavelength of (a) 532 nm and (b) 325 nm.

Table 2
The fitting G peak position, G FWHM, I_D/I_G, estimated L_a of the a-C films at 532 nm, and G peak dispersion with varying excitation wavelength.

Substrate bias (V)	G peak position (cm^{-1})	G FWHM (cm^{-1})	I_D/I_G	L_a (nm)	G peak dispersion (cm^{-1}/nm)
0	1549.5	178.5	1.73	1.77	0.19
−50	1544.0	180.3	2.05	1.93	0.09
−100	1544.7	182.0	1.92	1.87	0.15
−200	1546.2	190.0	1.46	1.62	0.23
−300	1544.3	191.4	1.63	1.72	0.16

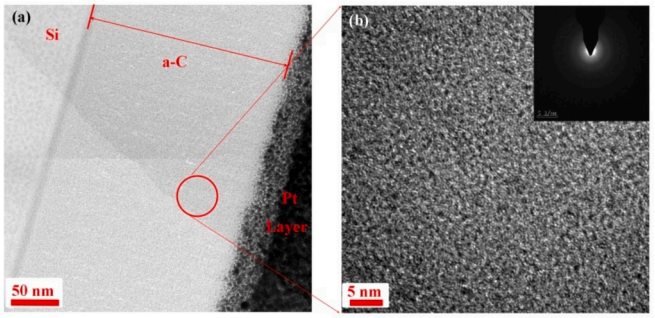

Fig. 4. (a) Cross-sectional TEM image, (b) HRTEM image and corresponding SAED of a-C film deposited at −50 V.

corresponding selected area electron diffraction (SAED) pattern of the a-C film deposited at −50 V. TEM analysis revealed that this sample had a thickness of approximately 200 nm, no nanocrystals were observed (Fig. 4a), and the corresponding SAED pattern just exhibited a diffusive ring (Fig. 4b), which was the characteristic of amorphous carbon films and agreed well with the aforementioned Raman spectra.

According to XPS, Raman and TEM, it is safe to deduce that typical a-C films with a stable sp^2/sp^3 ratio were prepared, and the size of sp^2 clusters can be adjusted by changing the applied negative bias from 0 to −300 V.

3.3. Electrical properties

First, I-V characteristics of a-C films were investigated, as shown in Fig. 5a. All I-V plots exhibited linear dependence, suggesting typical ohmic behavior in a-C films. Then, based on Hall-effect measurements, n-type conduction was identified in all a-C films, indicating that the carriers were negatively charged (i.e., electrons). Besides, the electron concentration and mobility of the a-C films were also investigated. Interestingly, in the bias range of 0 to −300 V, the electron concentration of the a-C films remained stable at approximately 2.1×10^{18} cm^{-3}, which was 1 or 2 orders of magnitude larger than that of amorphous Si (10^{16}–10^{17} cm^3) [27].

Considering that the distribution of sp^2 cluster can influence the electrical properties of a-C films, L_a, the room temperature resistivity (ρ_{RT}) and electron mobility were compared with various applied bias, as shown in Fig. 5b. Although L_a and ρ_{RT} of the a-C films showed irregular variations in the bias range of 0 to −300 V, they exhibited an obvious negative correlation. At −50 V, L_a reached its maximum value of 1.93

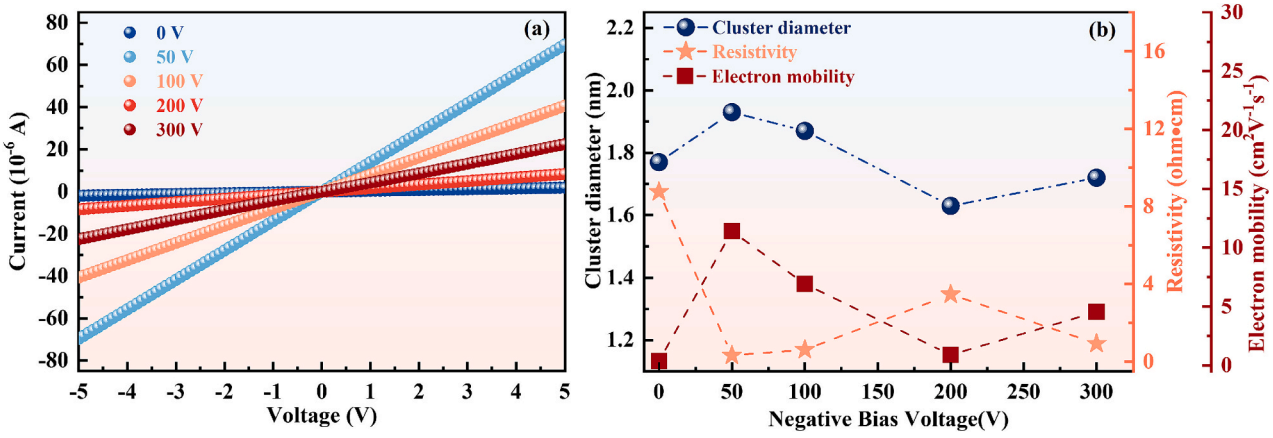

Fig. 5. (a) I-V characteristics, (b) sizes of sp^2 cluster, room temperature resistivity and electron mobility of a-C films deposited at various biases.

nm, while the corresponding ρ_{RT} reached its minimum value of 0.3 Ω•cm. As the bias increased to −300 V, L_a showed a decreasing trend, whereas ρ_{RT} increased monotonically. Additionally, the electron mobility in the samples changed remarkably from 0.4 to 11.4 $cm^2V^{-1}s^{-1}$ and exhibited a positive correlation with L_a. It was assumed that by adjusting the applied bias during deposition, the change of ρ_{RT} was caused by the variation of the electron mobility in the a-C films. This irregular variations of L_a and ρ_{RT} [52] may be explained from the HiPIMS [51], its higher degree of ionization and high-density plasma can result in various densification process in the subplantation deposition mechanism [53] and sp^2 cluster size.

To explore the dependence of their electrical properties on the test temperature, the I-V characteristics from 100 to 350 K were tested. Here, the resistances of the samples deposited at 0 V, −200 V and -300 V exceeded the upper limit of the PPMS, so their I-V characteristics were not present. In Fig. 6, both the two samples at −50 and -100 V showed the symmetric and linear I-V behaviors. As the temperature increased from 100 to 350 K, the corresponding voltage of each sample at a given excitation decreased evidently. For example, the voltage of sample at −100 V was 3.7 V at 350 K and dropped to 0.14 V at 100 K, as shown in Fig. 6b.

Then, the temperature dependence of dark resistivity (R-T) of the samples was investigated. In Fig. 7a, their resistivity monotonically decreased with increasing temperature, for instance, the resistivity of the sample at −50 V decreased evidently from 2.4 Ω•cm at 100 K to 0.1 Ω•cm at 350 K. At a certain temperature, the sample at −50 V exhibited a lower resistivity compared with the sample at −100 V, which was consistent with their room-temperature resistivity.

Generally, the R-T behaviors can reflect inherent transport properties in a-C films. Depending on their characteristics of the conductivity-temperature relationship, the dominant conduction mechanisms may involve Arrhenius-type conduction, VRH, or a combination of extended-state and hopping conduction [16,20,42,51]. Arrhenius behavior is common and can be judged from its activation energy, according to the following relation [16,43,44],

$$E_{act} = -k[d\ln(\sigma)/d(1/T)] \quad (2)$$

where E_{act} is the activation energy of a-C films, σ is the conductivity (that is, the multiplicative inverse of the resistivity), k is the Boltzmann constant, and T is the test temperature. As shown in Fig. 7b, E_{act} of the two samples evidently increased with increasing temperature: from 0.029 eV at 100 K to 0.065 eV at 350 K for the sample at −50 V, and from 0.032 eV at 100 K to 0.069 eV at 350 K for the sample at −100 V, respectively, suggesting that the temperature dependence of conductivity deviated from the Arrhenius behavior over the test temperature range from 100 to 350 K [16,42].

Referring to a classical cluster model [2,45,46] in a-C films, sp^2 clusters tend to be arranged in clusters embedded in the sp^3 matrix, and hopping between neighboring sp^2 clusters will determine its electrical behaviors [45–47]. In this work, the size of sp^2 clusters in those a-C films is less than 2 nm, while their thicknesses are around 200 nm. Thus, the a-C films can be treated as a three-dimensional (3D) composite material, with conductive sp^2 clusters distributed in the insulating sp^3 matrix. Furthermore, the 3D VRH transport mechanism may work under this condition.

The curves of Fig. 7a were replotted on a $T^{-1/4}$ temperature scale, as shown in Fig. 7c, and the measured data exhibited evident linear dependence on $T^{-1/4}$, which indicated a typical 3D VRH transport mechanism in the a-C films, with the following relationship [2,48,49],

$$\mathrm{Ln}(\sigma) \sim T^{-1/4} \quad (3)$$

3.4. Related carrier transport mechanism

Based on the above-mentioned analysis, the electrical behaviors of a-C films can be explained as follows. During deposition, with the applied negative bias increasing from 0 to −300 V, the stable sp^2/sp^3 ratio and the variable sp^2 cluster size were obtained in those a-C films, as proved by previous XPS and Raman measurements. This indicated that, at this lower energy range of the C particle, the sp^2 site can diffuse or condense into the sp^2 cluster in the sp^3 matrix [50]. From the Hall-effect measurement and R-T behaviors, both electronic conduction and the 3D VRH transport mechanism were confirmed. Thus, it was plausible that the resistivity of the a-C films was mainly controlled by electron hopping between neighboring sp^2 clusters, as shown in Fig. 8. For a-C films, the larger L_a and the higher degree of ordering can maximize the overlap integral of the wavefunctions, thereby achieving the higher electron mobility. So, the lowest resistivity of the a-C film at −50 V can be explained by the shortest average hopping distance between its largest sp^2 clusters and highest ordering, which may correspond to the largest electron mobility. With the applied bias increasing to −100 V and -300 V, though the L_a decreased, the more sp^2 clustering in the samples may be beneficial for electron hopping process, and result in their relatively higher electrical conductivity.

4. Conclusions

In summary, by precisely regulating the pulsed bias voltage with the high power impulse magnetron sputtering (HiPIMS) deposition method, we prepared a-C films with tailored sp^2 cluster sizes (L_a) ranging from 1.63 to 1.93 nm while maintaining a stable sp^2 content of approximately 52%. Comprehensive characterization revealed that all films exhibited n-type conductivity with a remarkably stable electron concentration of approximately 2.1×10^{18} cm^{-3}. The resistivity of the a-C films spanned 0.3–8.7 Ω·cm, where films with larger L_a values and higher structural

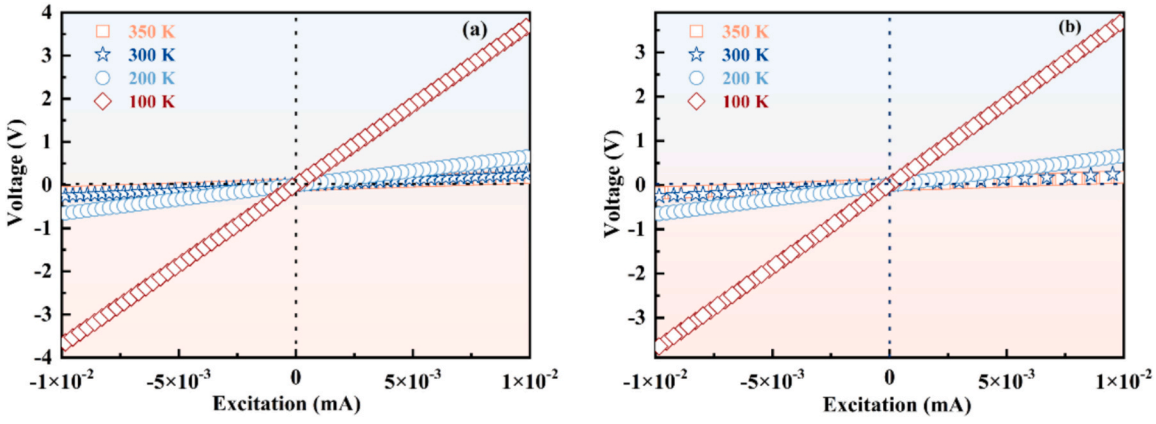

Fig. 6. I-V characteristics of a-C films deposited at −50 V (a) and -100 V (b), in the temperature range of 100 to 350 K.

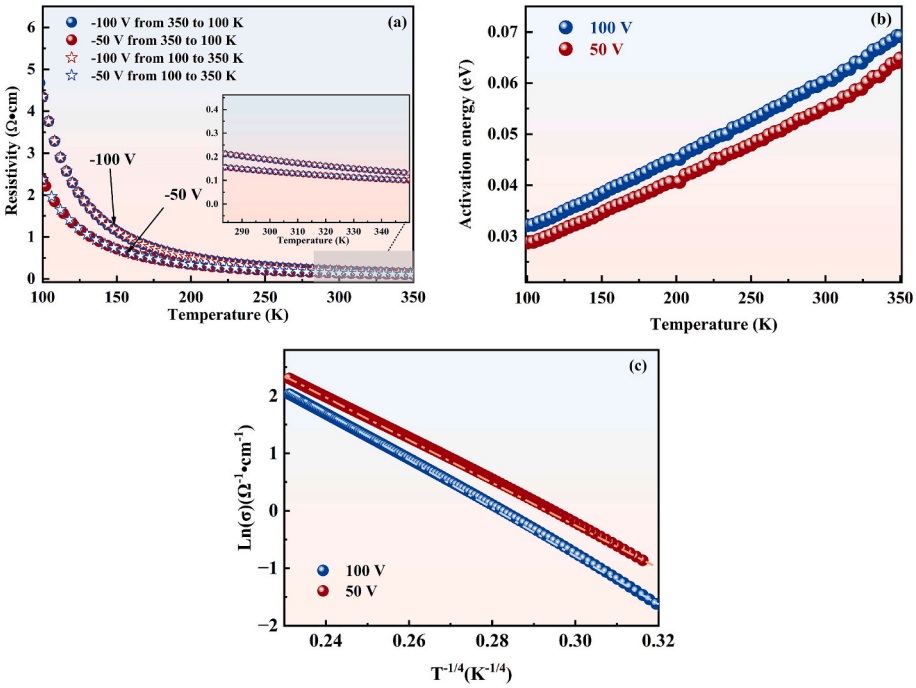

Fig. 7. (a) R-T behaviors of a-C films deposited at various biases, (b) variation of activation energy with temperature and (c) the relationship between Ln (σ) and $T^{-1/4}$ based on R-T data. And the dashed lines are inserted to guide the eyes in Fig. 7(c).

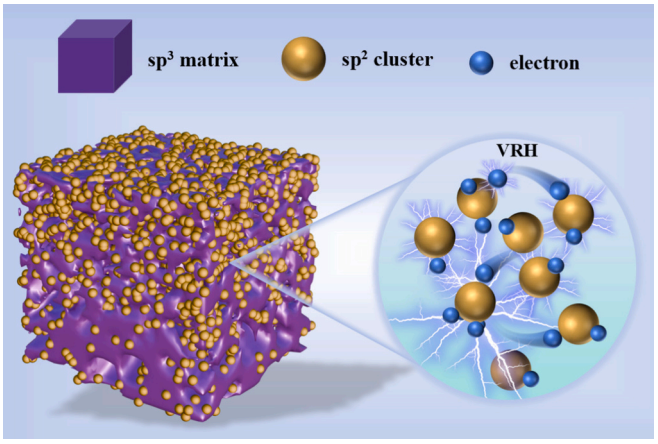

Fig. 8. Schematic diagram of VRH transport mechanism in a-C films.

ordering demonstrated reduced resistivity, attributed to enhanced electron mobility. The electron mobility exhibited a remarkable variation from 0.4 to 11.4 cm^2V^{-1} s^{-1} and showed a positive correlation with the sp^2 cluster size (L_a). The temperature dependence of dark resistivity (R-T) measurements further elucidated the transport mechanism. Their resistivity monotonically decreased with increasing temperature from 100 to 350 K. Critically, the linear dependence of Ln(σ) on $T^{-1/4}$ was observed. Additionally, the sp^2 cluster size (<2 nm) and the film thickness of approximately 200 nm enabled three-dimensional connectivity. The three-dimensional variable-range hopping (3D VRH) mechanism was confirmed as the dominant charge transport mechanism. This work not only addressed a critical gap in understanding their variable transport mechanisms but also provided new pathways for designing high-performance carbon-based electronic devices, such as MEMS sensors, resistive random access memory, and high-sensitivity photosensors.

CRediT authorship contribution statement

Jingyun Feng: Writing – original draft. **Peng Guo:** Writing – review & editing, Visualization, Validation, Project administration, Investigation, Funding acquisition, Formal analysis, Data curation, Conceptualization. **Hao Li:** Visualization, Investigation, Conceptualization. **Rende Chen:** Methodology, Investigation. **Aiying Wang:** Writing – review & editing, Visualization, Resources, Project administration, Funding acquisition.

Declaration of competing interest

The authors declare the following financial interests/personal relationships which may be considered as potential competing interests: Given her role as Editor of DRM journal, Aiying Wang had no involvement in the peer review of this article and had no access to information regarding its peer review. Full responsibility for the editorial process for this article was delegated to another journal editor.

If there are other authors, they declare that they have no known competing financial interests or personal relationships that could have appeared to influence the work reported in this paper.

Acknowledgements

This work was financially supported by the National Natural Science Foundation of China (52471105, U24A2030), Zhejiang Lingyan Research and Development Program (2024C01159), Leading Innovative and Entrepreneur Team Introduction Program of Zhejiang (2024R01004), Zhejiang Provincial Natural Science Foundation (LQN25E010007).

Data availability

Data will be made available on request.

References

[1] T. Huang, M. Yang, Y. Su, Y. Han, Q. Li, S. Zhang, T. Goto, R. Tu, L. Zhang, Molecular dynamics study on nano sliding behavior at DLC/AISI 304 interface, Carbon 240 (2025) 120371, https://doi.org/10.1016/j.carbon.2025.120371.

[2] J. Robertson, Diamond-like amorphous carbon, Mater. Sci. Eng. R-Rep. 37 (2002) 129–281, https://doi.org/10.1016/S0927-796X(02)00005-0.

[3] H. Liu, C. Li, Q. Ye, L. Chen, L. Qiao, Y. Yan, Inhibition mechanism of a diamond-like carbon (DLC) coating on the fretting crevice corrosion of stainless steel in artificial crevices, Corros. Sci. 253 (2025) 112995, https://doi.org/10.1016/j.corsci.2025.112995.

[4] A. Yazdanpanah, A.D. Pietri, A. Ben Hjal, M. Khodabakhshi, L. Biasiolo, M. Dabalà, Electrochemical and localized corrosion characteristics of kolsterised and DLC-coated 316LVM stainless steel for biomedical applications, Appl. Surf. Sci. 693 (2025) 162808, https://doi.org/10.1016/j.apsusc.2025.162808.

[5] M. Moseler, P. Gumbsch, C. Casiraghi, A.C. Ferrari, J. Robertson, The ultrasmoothness of diamond-like carbon surfaces, Science 309 (2005) 1545–1548, https://doi.org/10.1126/science.1114577.

[6] C-T. Toh, H. Zhang, J. Lin, A.S. Mayorov, Y.-P. Wang, C.M. Orofeo, D.B. Ferry, H. Andersen, N. Kakenov, Z. Guo, I.H. Abidi, H. Sims, K. Suenaga, S.T. Pantelides, B. Özyilmaz, Synthesis and properties of free-standing monolayer amorphous carbon, Nature 577 (2020) 199–203, https://doi.org/10.1038/s41586-019-1871-2.

[7] I. Kim, C. Shim, S.W. Kim, C. Lee, J. Kwon, K. Byun, U. Jeong, Amorphous carbon films for electronic applications, Adv. Mater. 35 (2023) 2204912, https://doi.org/10.1002/adma.202204912.

[8] S. Liu, Z. Zhao, W. Zhang, R. Chen, J. Wei, P. Guo, A. Wang, Micron-scale al particulates to improve the piezoresistive performance of amorphous carbon films, Diam. Relat. Mater. 143 (2024) 110926, https://doi.org/10.1016/j.diamond.2024.110926.

[9] J. Zhou, P. Guo, L. Cui, C. Yan, D. Xu, F. Li, C. Zhang, A. Wang, Wrinkled and cracked amorphous carbon film for high-performance flexible strain sensors, Diam. Relat. Mater. 132 (2023) 109619, https://doi.org/10.1016/j.diamond.2022.109619.

[10] H. Tian, Y. Ma, Z. Li, M. Cheng, S. Ning, E. Han, M. Xu, P.-F. Zhang, K. Zhao, R. Li, Y. Zou, P. Liao, S. Yu, X. Li, J. Wang, S. Liu, Y. Li, X. Huang, Z. Yao, D. Ding, J. Guo, Y. Huang, J. Lu, Y. Han, Z. Wang, Z.G. Cheng, J. Liu, Z. Xu, K. Liu, P. Gao, Y. Jiang, L. Lin, X. Zhao, L. Wang, X. Bai, W. Fu, J.-Y. Wang, M. Li, T. Lei, Y. Zhang, Y. Hou, J. Pei, S.J. Pennycook, E. Wang, J. Chen, W. Zhou, L. Liu, Disorder-tuned conductivity in amorphous monolayer carbon, Nature 615 (2023) 56–61, https://doi.org/10.1038/s41586-022-05617-w.

[11] P.Y. Le, A. Gazzana, B.J. Murdoch, D.G. McCulloch, D.R. McKenzie, H.N. Tran, J. G. Partridge, Room-temperature negative differential resistance in amorphous carbon: the role of electron trapping defects at device interfaces, IEEE Trans. Electron Devices 68 (2021) 720–725, https://doi.org/10.1109/TED.2020.3044021.

[12] Z.C. Zhao, T.J. Raeber, B.J. Murdoch, J.G. Partridge, D.G. McCulloch, D. R. McKenzie, Unifying the optical and electrical properties of amorphous carbon: application to hopping photoconductivity and memristance, J. Appl. Phys. 128 (2020), https://doi.org/10.1063/5.0024224.

[13] X. Ma, P. Guo, X. Tong, Y. Zhao, Q. Zhang, P. Ke, A. Wang, Piezoresistive behavior of amorphous carbon films for high performance MEMS force sensors, Appl. Phys. Lett. 114 (2019) 253502, https://doi.org/10.1063/1.5096225.

[14] G. Zhou, Z. Ren, L. Wang, J. Wu, B. Sun, A. Zhou, G. Zhang, S. Zheng, S. Duan, Q. Song, Resistive switching memory integrated with amorphous carbon-based nanogenerators for self-powered device, Nano Energy 63 (2019) 103793, https://doi.org/10.1016/j.nanoen.2019.05.079.

[15] E.C. Ahn, H.S.P. Wong, E. Pop, Carbon nanomaterials for non-volatile memories, Nat. Rev. Mater. 3 (2018) 18009, https://doi.org/10.1038/natrevmats.2018.9.

[16] S. Bhattacharyya, S.R.P. Silva, Transport properties of low-dimensional amorphous carbon films, Thin Solid Films 482 (2005) 94–98, https://doi.org/10.1016/j.tsf.2004.11.125.

[17] L. Zhang, X. Wei, Y. Lin, F. Wang, A ternary phase diagram for amorphous carbon, Carbon 94 (2015) 202–213, https://doi.org/10.1016/j.carbon.2015.06.055.

[18] X. Zhou, T. Suzuki, H. Nakajima, K. Komatsu, K. Kanda, H. Ito, H. Saitoh, Structural analysis of amorphous carbon films by spectroscopic ellipsometry, RBS/ERDA, and NEXAFS, Appl. Phys. Lett. 110 (2017) 201902, https://doi.org/10.1063/1.4983643.

[19] Y. Katamune, S. Takeichi, S. Ohmagari, T. Yoshitake, Hydrogenation effects on carrier transport in boron-doped ultrananocrystalline diamond/amorphous carbon films prepared by coaxial arc plasma deposition, J. Vac. Sci. Technol. A 33 (2015), https://doi.org/10.1116/1.4931062.

[20] Z. Zhai, H. Shen, J. Chen, Fast growth of conductive amorphous carbon films by HFCVD with filament temperature control, Mater. Lett. 228 (2018) 293–296, https://doi.org/10.1016/j.matlet.2018.06.039.

[21] N. Dwivedi, S. Kumar, H.K. Malik, Govind, C.M.S. Rauthan, O.S. Panwar, Correlation of sp^3 and sp^2 fraction of carbon with electrical, optical and nano-mechanical properties of argon-diluted diamond-like carbon films, Appl. Surf. Sci. 257 (2011) 6804–6810, https://doi.org/10.1016/j.apsusc.2011.02.134.

[22] E. Mohagheghpour, M. Rajabi, R. Gholamipour, M.M. Larijani, S. Sheibani, Correlation study of structural, optical and electrical properties of amorphous carbon thin films prepared by ion beam sputtering deposition technique, Appl. Surf. Sci. 360 (2016) 52–58, https://doi.org/10.1016/j.apsusc.2015.10.213.

[23] Z. Zhai, H. Shen, J. Chen, Y. Jiang, Q. Tang, Investigation of substrate temperature and cooling method on the properties of amorphous carbon films by hot-filament CVD with acetylene, Carbon 117 (2017) 322–330, https://doi.org/10.1016/j.carbon.2017.03.006.

[24] R.U.R. Sagar, X. Zhang, C. Xiong, Y. Yu, Semiconducting amorphous carbon thin films for transparent conducting electrodes, Carbon 76 (2014) 64–70, https://doi.org/10.1016/j.carbon.2014.04.049.

[25] A. Tibrewala, E. Peiner, R. Bandorf, S. Biehl, H. Lüthje, Transport and optical properties of amorphous carbon and hydrogenated amorphous carbon films, Appl. Surf. Sci. 252 (2006) 5387–5390, https://doi.org/10.1016/j.apsusc.2005.12.046.

[26] M. Doyama, A. Ichida, Y. Inoue, Y. Kogure, T. Nozaki, S. Yamada, Electrical properties of amorphous carbon films, Scr. Mater. 44 (2001) 1191–1194, https://doi.org/10.1016/S1359-6462(01)00680-7.

[27] T. Soga, T. Jimbo, K. Krishna, M. Umeno, Amorphous carbon thin films for optoelectric device application, Int. J. Mod. Phys. B 14 (2000) 206–217, https://doi.org/10.1142/s0217979200000200.

[28] X. Zuo, P. Ke, R. Chen, X. Li, M. Odén, A. Wang, Discharge state transition and cathode fall thickness evolution during chromium HiPIMS discharge, Phys. Plasmas 24 (2017), https://doi.org/10.1063/1.4995482.

[29] M. Huang, X. Zhang, P. Ke, A. Wang, Graphite-like carbon films by high power impulse magnetron sputtering, Appl. Surf. Sci. 283 (2013) 321–326, https://doi.org/10.1016/j.apsusc.2013.06.109.

[30] X. Zuo, R. Chen, P. Ke, A. Wang, Gas breakdown and discharge formation in high-power impulse magnetron sputtering, IEEE Trans. Plasma Sci. 47 (2019) 1215–1222, https://doi.org/10.1109/TPS.2018.2889696.

[31] J. Díaz, G. Paolicelli, S. Ferrer, F. Comin, Separation of the sp^3 and sp^2 components in the C1s photoemission spectra of amorphous carbon films, Phys. Rev. B 54 (11) (1996) 8064–8069, https://doi.org/10.1103/PhysRevB.54.8064.

[32] P. Mérel, M. Tabbal, M. Chaker, S. Moisa, J. Margot, Direct evaluation of the sp^3 content in diamond-like-carbon films by XPS, Appl. Surf. Sci. 136 (1998) 105–110, https://doi.org/10.1016/S0169-4332(98)00319-5.

[33] G. González-Díaz, D. Pastor, E. García-Hemme, D. Montero, R. García-Hernansanz, J. Olea, et al., A robust method to determine the contact resistance using the van der Pauw set up, Measurement 98 (2017) 151–158, https://doi.org/10.1016/j.measurement.2016.11.040.

[34] S. Nakao, K. Yukimura, S. Nakano, H. Ogiso, DLC coating by HiPIMS: the influence of substrate bias voltage, IEEE Trans. Plasma Sci. 41 (2013) 1819–1829, https://doi.org/10.1109/TPS.2013.2256800.

[35] J.G. Buijnsters, L. Vázquez, Influence of external bias on the surface morphology of a-C:H films grown by electron cyclotron resonance chemical vapor deposition, Surf. Coat. Technol. 201 (2007) 8950–8954, https://doi.org/10.1016/j.surfcoat.2007.03.055.

[36] P. Guo, X. Li, L. Sun, R. Chen, P. Ke, A. Wang, Stress reduction mechanism of diamond-like carbon films incorporated with different Cu contents, Thin Solid Films 640 (2017) 45–51, https://doi.org/10.1016/j.tsf.2017.09.001.

[37] I. Ahmad, S.S. Roy, P.D. Maguire, P. Papakonstantinou, J.A. McLaughlin, Effect of substrate bias voltage and substrate on the structural properties of amorphous carbon films deposited by unbalanced magnetron sputtering, Thin Solid Films 482 (2005) 45–49, https://doi.org/10.1016/j.tsf.2004.11.158.

[38] A.C. Ferrari, J. Robertson, A.C. Ferrari, J. Robertson, Raman spectroscopy of amorphous, nanostructured, diamond–like carbon, and nanodiamond, Phil. Trans. R. Soc. Lond. A. 362 (2004) 2477–2512, https://doi.org/10.1098/rsta. 2004.1452.

[39] A.C. Ferrari, J. Robertson, Interpretation of Raman spectra of disordered and amorphous carbon, Phys. Rev. B 61 (2000) 14095–14107, https://doi.org/10.1103/PhysRevB.61.14095.

[40] Z. Zhai, H. Shen, J. Chen, X. Li, Effect of deposition pressure on the properties of amorphous carbon films by hot-filament chemical vapor deposition, J. Mater. Sci. Mater. Electron. 30 (2019) 10145–10151, https://doi.org/10.1007/s10854-019-01350-9.

[41] M. Khadem, O.V. Penkov, V.E. Pukha, M.V. Maleyev, D-E. Kim, Ultra-thin nano-patterned wear-protective diamond-like carbon coatings deposited on glass using a C_{60} ion beam, Carbon 80 (2014) 534–543, https://doi.org/10.1016/j.carbon.2014.08.093.

[42] S.H. Moustafa, M. Koós, I. Pócsik, DC electrical properties of amorphous carbon with different bonding hybridization, J. Non-Cryst. Solids 227-230 (1998) 1087–1091, https://doi.org/10.1016/S0022-3093(98)00253-1.

[43] S. Bhattacharyya, Observation of delocalized transport and low-dimensionality effects in disordered carbon thin films, Appl. Phys. Lett. 91 (2007), https://doi.org/10.1063/1.2790844.

[44] M. Koós, S.H.S. Moustafa, E. Szilágyi, I. Pócsik, Non-Arrhenius temperature dependence of direct-current conductivity in amorphous carbon (a-C:H) above room temperature, Diam. Relat. Mater. 8 (1999) 1919–1926, https://doi.org/10.1016/S0925-9635(99)00165-X.

[45] Y. Miyajima, A.A.D.T. Adikaari, S.J. Henley, J.M. Shannon, S.R.P. Silva, Electrical properties of pulsed UV laser irradiated amorphous carbon, Appl. Phys. Lett. 92 (2008), https://doi.org/10.1063/1.2908208.

[46] R.U.A. Khan, J.D. Carey, S.R.P. Silva, B. Jones, R.C. Barklie, Electron delocalization in amorphous carbon by ion implantation, Phys. Rev. B 63 (2001) 1212011–1212014.

[47] M. Chhowalla, A.C. Ferrari, J. Robertson, G.A.J. Amaratunga, Evolution of sp^2 bonding with deposition temperature in tetrahedral amorphous carbon studied by Raman spectroscopy, Appl. Phys. Lett. 76 (2000) 1419–1421, https://doi.org/10.1063/1.126050.

[48] C. Godet, Physics of bandtail hopping in disordered carbons, Diam. Relat. Mater. 12 (2003) 159–165, https://doi.org/10.1016/S0925-9635(03)00017-7.

[49] N.F. Mott, Conduction in non-crystalline materials, Philos. Mag. 19 (1969) 835–852, https://doi.org/10.1080/14786436908216338.

[50] A. Ilie, A.C. Ferrari, T. Yagi, J. Robertson, Effect of sp^2-phase nanostructure on field emission from amorphous carbons, Appl. Phys. Lett. 76 (2000) 2627–2629, https://doi.org/10.1063/1.126430.
[51] R.K. Tripathi, O.S. Panwar, I. Rawal, C.K. Dixit, A. Verma, P. Chaudhary, A. K. Srivastava, B.C. Yadav, Study of variable range hopping conduction mechanism in nanocrystalline carbon thin films deposited by modified anodic jet carbon arc technique: application to light-dependent resistors, J. Mater. Sci. Mater. Electron. 32 (2021) 2535–2546, https://doi.org/10.1007/s10854-020-05020-z.
[52] R. Yuan, Y. Guo, I. Gurgan, N. Siddique, Y-S. Li, S. Jang, G.A. Noh, S.H. Kim, Raman spectroscopy analysis of disordered and amorphous carbon materials: a review of empirical correlations, Carbon 238 (2025) 120214, https://doi.org/10.1016/j.carbon.2025.120214.
[53] J. Robertson, Diamond-like amorphous carbon, Mater. Sci. Eng. R 37 (2002) 129–281, https://doi.org/10.1016/S0927-796X(02)00005-0.